SCIENTIFIC REPORTS

OPEN

SUBJECT AREAS:
MAGNETIC DEVICES
MAGNETIC PROPERTIES AND MATERIALS
APPLIED PHYSICS

Received
20 February 2014

Accepted
7 May 2014

Published
27 May 2014

Correspondence and requests for materials should be addressed to Z.B.S. (a0018876@nus.edu.sg)

Topological state transport in topological insulators under the influence of hexagonal warping and exchange coupling to in-plane magnetizations

Z. B. Siu[1,2,3], M. B. A. Jalil[1,3] & S. G. Tan[2,3]

[1]NUS Graduate School for Integrative Sciences and Engineering, National University of Singapore, [2]Data Storage Institute, Agency for Science, Technology and Research, [3]Computational Nanoelectronics and Nano-device Laboratory, Electronic and Computer Engineering Department, National University of Singapore.

A hexagonal warping term has been proposed recently to explain the experimentally observed 2D equal energy contours of the surface states of the topological insulator Bi_2Te_3. Differing from the Dirac fermion Hamiltonian, the hexagonal warping term leads to the opening up of a band gap by an *in-plane* magnetization. We study the transmission between two Bi_2Te_3 segments subjected to different in-plane magnetizations and potentials. The opening up of a bandgap, and the accompanying displacement and distortion of the constant energy surfaces from their usual circular shapes by the in-plane magnetizations, modify the transverse momentum overlap between the two Bi_2Te_3 segments, and strongly modulate the transmission profile. The strong dependence of the TI surface state transport of Bi_2Te_3 on the magnetization orientation of an adjacent ferromagnetic layer may potentially be utilized in, e.g., a memory readout application.

Topological insulators (TIs)[1] are a relatively new class of materials which have attracted much attention due to their rich physics. For example, Majorana fermions have been shown to exist in junctions between superconductors and ferromagnetic insulators deposited on top of TIs[2–4]. Furthermore, strong spin orbit coupling leads to interesting effects when a magnetization is applied to a TI[5–7]. In particular, Yokoyama and colleagues studied the magnetoresistance in a two dimensional junction between two ferromagnets magnetized in different directions deposited on top of a topological insulator[8]. They found that the transmission at a given energy is strongly influenced by the relative k-space displacements of the Fermi surfaces resulting from the differing magnetizations. The influence of the Fermi surfaces on the magnetoresistance motivates the study of the topological insulator Bi_2Te_3 in this present work.

The experimentally observed[9,10] 2D equal energy contours (EECs) of the surface states in Bi_2Te_3 differ at high Fermi energies from the circular Dirac cone predicted by the simple Dirac fermion Hamiltonian $H = v\vec{k} \times \vec{\sigma}$. At low Fermi energies, the EEC takes the form of a circle (Fig. 1(a)). As the Fermi energy increases, the contour evolves from a circle to a hexagon and then to a snowflake with sharp tips along the six ΓM directions. Based on the underlying 3-fold rotational and two-fold mirror symmetry of the [111] surface of the underlying rhombohedral Bi_2Te_3 crystal structure, Fu suggested the addition of a hexagonal warping term to the Hamiltonian[11]. The Hamiltonian then takes the form of

$$H = v\left(k_x\sigma_y - k_y\sigma_x\right) + \lambda\sigma_z\left(k_x^3 - 3k_xk_y^2\right), \tag{1}$$

where x is in the ΓK direction. The Hamiltonian reproduces the experimentally measured EECs.

Unlike the Dirac cone which is rotationally symmetric about the k_x, k_y plane, the dispersion relation arising from Eq. 1 has only 6 fold rotational symmetry. The anisotropy of the Fermi surface in the k_x, k_y plane can be expected to give rise to interesting directional dependent effects. For example, it has been suggested that a Bi_2Te_3 segment with a potential step may be exploited as a flat lens for focusing electron beams[12].

Another peculiarity of the Hamiltonian is that an *in-plane* magnetic field modeled by a Zeeman term can open up a band gap[11]. The Zeeman term mathematically resembles that due to magnetic coupling to a proximate

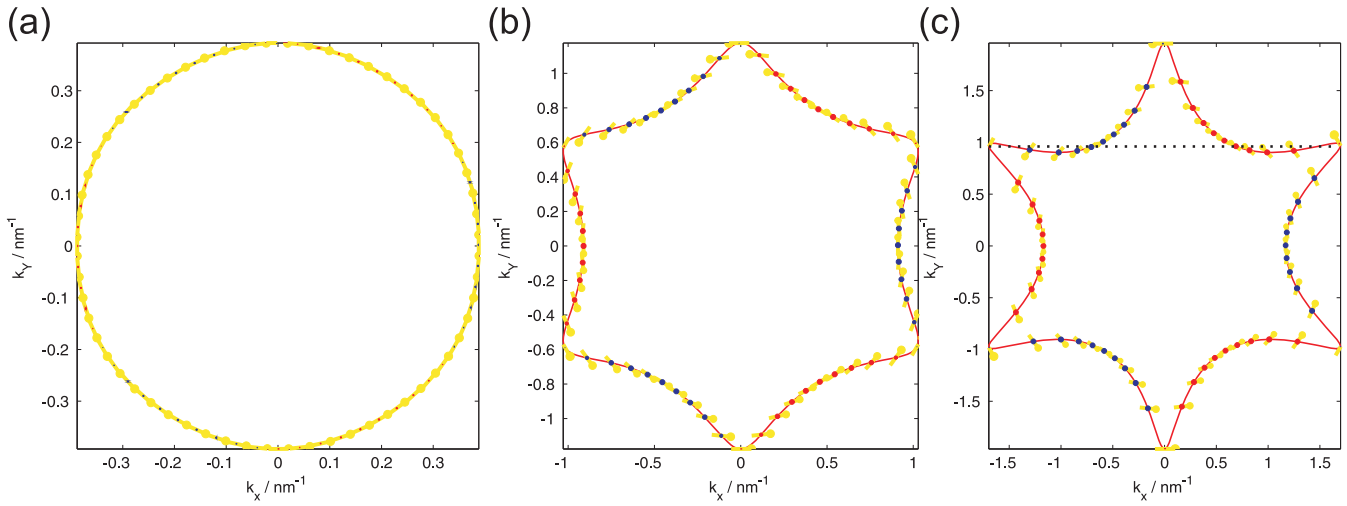

Figure 1 | The EECs and eigenstate spin orientations for $E =$ (a) 0.1 eV, (b) 0.3 eV and (c) 0.5 eV. The green arrows on the EECs indicate the orientation of the $\langle\sigma_x\rangle$ and $\langle\sigma_y\rangle$ components at each point on the contour with larger arrowheads indicating higher spin polarization. The red and blue dots indicate the $\langle\sigma_z\rangle$ polarization with larger dots indicating larger magnitudes of spin polarization. Blue (red) dots indicate positive (negative) spin z polarization. The dotted line in panel (c) indicates one value of k_y where there are six real values of k_x.

ferromagnetic film or the effects of magnetic doping[13]. For ease of exposition we say that the Zeeman term arises from an external magnetization. We write the Zeeman term as $\vec{M}\cdot\vec{\sigma}$ and collect the appropriate coupling constants into $\vec{M}$ itself. The introduction of a bandgap due to an in-plane magnetization differs from the simple Dirac fermion Hamiltonian $H = v\vec{k}\times\vec{\sigma}$ where only an *out-of-plane* magnetization can open up a band gap. We find that besides opening up a band gap and displacing the position of the Dirac points in reciprocal space, the in-plane magnetic field also distorts the shape of the constant energy surfaces.

Despite the interesting bandstructure properties of Bi_2Te_3, transport across Bi_2Te_3 segments has not yet been studied extensively. Ref. 14 derived the transmission between one TI segment and another with an externally applied step-edge potential $V(x) = -V_0\theta(-x)$ where $\theta(x)$ is the Heaviside step function. In the derivation it was implicitly assumed that there is a propagating state in the transmitted segment which satisfies energy and transverse momentum conservation. However, there exists more than one propagating state with real, positive k_x for some values of k_y at high $|E - V|$ (see Fig. 1(c)). It is not evident which of these multiple values of k_x in the transmitted region should be chosen. Moreover, the derivation matched only the wavefunctions, and not the probability flux, across the interface. Ref. 16 considered the transmission of a wave incident from $x < 0$ across a Dirac delta potential located at $x = 0$. The transmitted wavefunction at $x > 0$ contains *left* propagating components back into the incident region within the $\sin(k_x x)$ and $\cos(k_x x)$ terms in Eq. (4) of the paper. The presence of backwards propagating wave components in the transmitted region is counter-intuitive.

For a given value of transverse momentum k_y and Fermi energy E, the Hamiltonian Eq. 1 admits six eigenstates with real or imaginary k_x which may be real or complex, and which come in three Kramers time-reversal pairs. We consider the transmission of electrons traveling in the $+x$ direction from one Bi_2Te_3 segment on the left to another on its right. Three of the eigenstates propagate or decay in the $+x$ direction, and are physically appropriate states in the segment which a wave traveling in the $+x$ direction is transmitted into. The other three eigenstates propagate or decay in the $-x$ direction, and are physically appropriate as the reflected components of a wavefunction in the incident segment. Both Refs. 14 and 16 assume that an incident energy eigenstate with wavevector k_x be reflected at the interface into an eigenstate with the wavevector $-k_x$. This imposes an artificial constraint that the incident wave is not reflected back into the other 2 eigenstates which also propagate or decay in the correct direction.

One difficulty in considering all eigenstates in studying transmission across an interface between 2 Bi_2Te_3 TI segments is the issue of boundary conditions. In each TI segment there are 6 eigenstates for a given value of E and transverse momentum k_y. In solving the transmission problem across an interface from TI region I to region II, the weightages of six of the twelve eigenstates involved are fixed by the requirements that evanescent states decay away from the interface, and that the state incident on the interface from region I is given. This leaves the weightages of the remaining 6 states to be solved for. The usual practice of matching the wavefunctions and first derivatives for the two spinor components across an interface between the two TI segments gives only 4 equations. Another boundary condition besides wavefunction and first derivative continuity is required to solve for the 6 unknowns uniquely. We note that more recent works[15,17] did consider all six eigenstates explicitly. However, Ref. 15 only considered transmission across a delta potential barrier, whereas it is not clear from the paper what set of boundary conditions Ref. 17 used.

To the best of our knowledge, transport across Bi_2Te_3 segments magnetized in different directions has not yet been studied. In this work, we show that probability flux conservation across the interface requires that the matching of the second derivatives of the wavefunctions across the interface. We then calculate the transmission between two Bi_2Te_3 segments subjected to different external potentials and magnetic fields. We find that the distortion and displacement of the constant energy surfaces, and the opening up of a band gap lead to a rich transmission profile as the magnetization directions and energy are varied.

Methods

Boundary conditions. We consider a generic Hamiltonian of the form

$$\begin{aligned}\hat{H} &= a\hat{p}_x + b\hat{p}_x^2 + c\hat{p}_x^3 + d \\ &= -ia\partial_x - b\partial_x^2 + ic\partial_x^3 + d.\end{aligned} \tag{2}$$

The a, b, c and d above may be numbers or Hermitian operators which commute with $\hat{p}_x$, for example some combinations of $\vec{\sigma}$ or $\hat{p}_y$ and are independent of p_x. For this Hamiltonian, we have $\hat{v}_x = \dfrac{\partial\hat{H}}{\partial\hat{p}_x} = a + 2b\hat{p}_x + 3c\hat{p}_x^2$. Explicitly expanding out $\partial_t\rho$ gives, after some manipulations of the x derivatives and integration by parts,

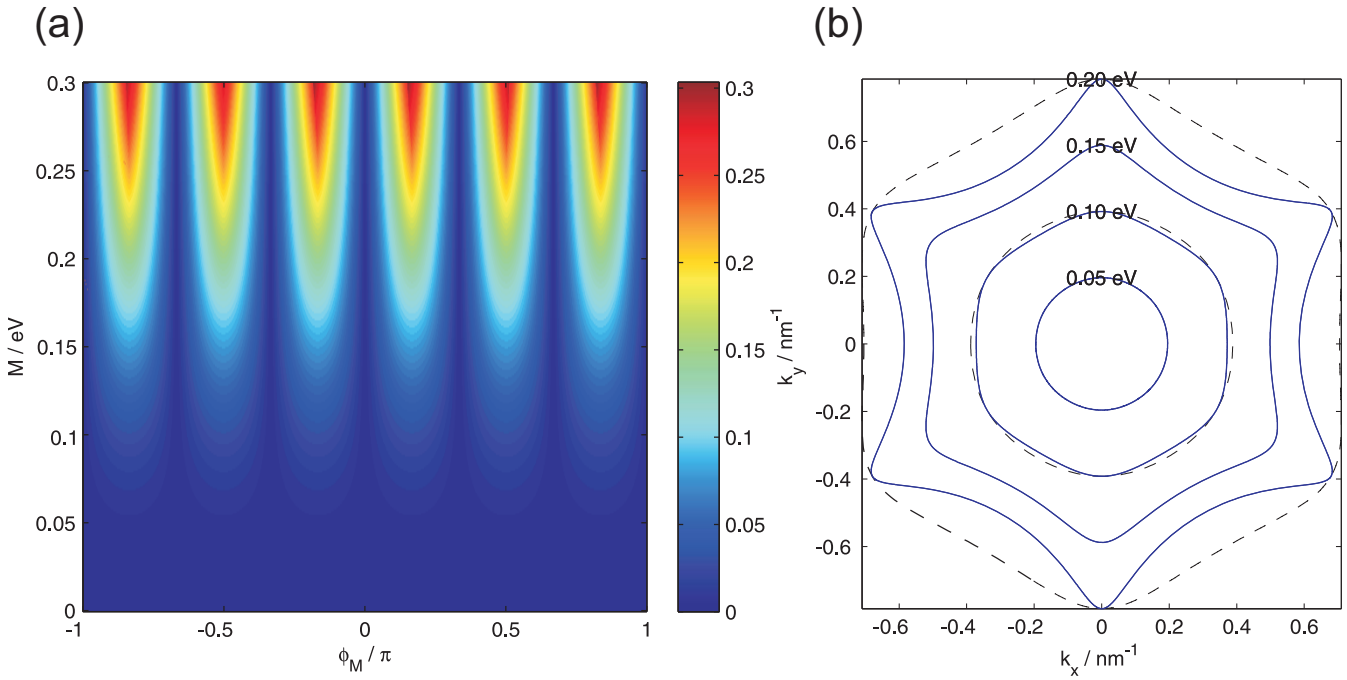

Figure 2 | (a) The band gap in eV as a function of the magnetic field strength M and angle ϕ_M. (b) The thick blue lines indicate the trajectory of the Dirac points in k space as ϕ_M is varied at fixed values of M from 0.05 eV to 0.20 eV. The black dotted lines show the constant energy surfaces at $E = 0.1$ eV and $E = 0.2$ eV.

$$\partial_t \rho = i\left((\hat{H}\psi)^*\psi - \psi^*(\hat{H}\psi)\right) = -\partial_x\left(\psi^* a\psi + 2\mathrm{Im}(\psi^* b\partial_x\psi) - 2\mathrm{Re}\left(\psi^* c\partial_x^2\psi\right) + (\partial_x\psi^*)c(\partial_x\psi)\right). \quad (3)$$

Comparing with the continuity equation $\partial_t\rho + \partial_x j = 0$, we recognize the terms within the large brackets in the second line as the probability flux. If $c = 0$ (i.e. the Hamiltonian is only quadratic in $\hat{p}_x$), the flux is the real part of $\psi^*\hat{v}\psi$ so that for a Hamiltonian quadratic in $\hat{p}_x$, matching $\psi^*\hat{v}\psi$ across an interface – which matches both the real and imaginary parts – automatically matches the flux across both sides of an interface.

However, for $c \neq 0$, the real part of the c term in $\psi^*\hat{v}\psi$ is $3\mathrm{Re}\left(\psi^* c\partial_x^2\psi\right)$ which is not, in general, equal to the c term in the flux, $2\mathrm{Re}\left(\psi^* c\partial_x^2\psi\right) - \partial_x\psi^* c\partial_x\psi$. A simple example suffices to illustrate this. Putting $c = 1$ for simplicity, and writing $\psi = \exp(ikx)$ where $k = (k_r + ik_i)$ is in general complex, we have at $x = 0$, we have $3\mathrm{Re}\left(\psi^* c\partial_x^2\psi\right) = -3\left(k_r^2 - k_i^2\right)$ which is not equal to $2\mathrm{Re}\left(\psi^* c\partial_x^2\psi\right) - \partial_x\psi^* c\partial_x\psi = -3k_r^2 + 2k_i^2$ if the wavevector has an imaginary part.

In the system we will be considering in this paper, we identify the operators $a = v\sigma_y - 3k_y^2\lambda\sigma_z$, $b = 0$, and $c = \lambda\sigma_z$ across both sides of the interface. (They differ in the d term of Eq. 2.) In this instance, flux conservation can be achieved by matching i) ψ ii) $\partial_x\psi$ and iii) $\partial_x^2\psi$ across both sides of the interface.

Results

Equal energy contours under an in-plane magnetization. The eigenenergy E for a given $\vec{k} = k(\cos(\phi), \sin(\phi), 0)$ and magnetization $\vec{M} = M(\cos(\phi_M), \sin(\phi_M), 0)$ reads

$$E^2 = \frac{1}{2}\left(k^6\lambda^2(1 + \cos(6\phi)) + 2k^2v^2 + 2M^2 - 4Mkv\sin(\phi - \phi_m)\right). \quad (4)$$

The high powers of k and presence of trigonometric terms involving ϕ and ϕ_M present difficulties for the derivation of compact analytic expressions for the band gap and position of the Dirac point in k-space at which the lowest energy propagating particle state with real $\vec{k}$ exist. We calculate these quantities numerically. We use the numerical values of $v = 25.5$ eVnm and $\lambda = 0.25$ eVnm^{-3} [11].

The in-plane magnetization leads to the opening up of a band gap and a displacement of the Dirac point, as shown in panels (a) and (b) of Fig. 2 respectively. The band gap reaches its maximum value of M at magnetization angles $\phi_M = \pm(2n-1)\pi/6$, $n = 1, 2, 3$, and varies in a roughly sinusoidal manner with the magnetization angle. The band gap shifts the minimum energy at which propagating particle states exist upwards. This leads to the k-space area covered by the EEC at a given energy being generally larger for a magnetization angle with a smaller band gap compared to that of a magnetization angle with a larger band gap. This fact will have consequences for charge transport between Bi_2Te_3 segments magnetized in different directions.

The trajectory of the Dirac points for a given magnetization magnitude as the magnetization angle is varied follows a more complicated path than the circular trajectories of the simple Dirac fermion Hamiltonian. For the latter, the trajectories form circles in k-space. In Bi_2Te_3, the trajectories of the Dirac points resemble the shapes of the EECs. The trajectories of the Dirac points exhibit greater distortion from the circular shape at a given value of M than the EECs do for $E = M$.

The positions of the Dirac points $\vec{k}^*$ differ from the $\vec{k}^* = \hat{z} \times \vec{M}/v$ given in Ref. 11. The latter holds only in the low M limit when the trajectories of the Dirac points are roughly circular. The k-space angle $\phi = \arctan(k_y/k_x)$ of the Dirac point is related to the magnetization angle by $\phi_M = \phi - \pi/2$. This can be seen from the last term of Eq. 4 where the energy achieves its minimum value for fixed values of k and M when the $\sin(\phi - \phi_M)$ term is 1. At $\phi = \phi_M + \pi/2$ and the large k limit, the k^6 term of Eq. 4 dominates so that $E \approx k^3\lambda|\sin(3\phi_M)|$. This explains the peaking of sinusoidal variation and peaking of the band gap at $\phi_M = \pm(2n-1)\pi/6$, $n = 1, 2, 3$.

Transport between two Bi_2Te_3 segments. To study the effects of the in-plane magnetization on the transport properties of Bi_2Te_3, we consider the system outlined schematically in Fig. 3. The system consists of two Bi_2Te_3 segments of semi-infinite length along the x direction and infinite width along the y direction. Charge flows from the left source segment to the right drain segment in which a magnetization $\vec{M}_2 = M_2(\cos(\phi_{M2}), \sin(\phi_{M2}))$ and a potential U is applied. The potential shifts the dispersion relation of the drain segment on the energy axis with respect to that of the source segment. For a given source Fermi energy E we define $E_2 = E - U$.

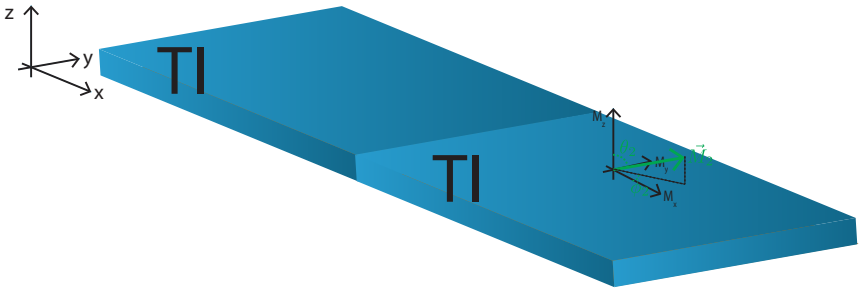

Figure 3 | A schematic of the system studied. The system consists of two semi-infinite long Bi_2Te_3 segments of infinite width. Charge flows from the left source segment into the right drain segment in which a magnetization $\vec{M}_2$ and external potential U is applied.

Fig. 4 shows the transmission plotted as a function of magnitude M_2 and direction ϕ_{M2} of the drain magnetization for the transmission from an unmagnetized source segment. The electron energy is chosen to be the intermediate range, i.e., $E = 0.3$ eV, at which the EEC takes the form of a hexagon, while the drain segment is biased at $E_2 = E - U_2 = 0.1$ eV, i.e., at the low energy regime where the EEC assumes a circular shape.

The dependence of the transmission on M_2 can be divided into three regimes. In the low M_2 regime (0 eV $< M_2 <$ 0.07 eV) the transmission peaks weakly around $\phi_{M2} = \pm\pi/2$, while at intermediate values of M_2 the transmission exhibits sharper peaks near $\phi_{M2} = 0, \pm\pi$. At large values of M_2, the trend is reversed and the transmission drops to almost zero near $\phi_{M2} = \pm n\pi/6$, $n = (1, 3, 5)$.

Discussion

These observations may be explained by examining the evolution of the EECs as M_2 and ϕ_{M2} are varied (as shown in Fig. 5).

For low values of M_2, the EECs at the drain lie completely within the k-space region spanned by the EEC at the source. Fig. 5(a) shows that the drain EECs adopt an almost circular profile and the k_y range spanned is only weakly dependent on ϕ_{M2}. The spin polarizations (not shown) of the right-propagating eigenstates also do not exhibit much angular variation. Thus, there is little modulation of the transmission as the orientation of M_2 is varied. In the intermediate range of M_2 [shown in Fig. 5(b)], the transmission is dominated by the k_y range spanned by the drain EEC. Since the transverse momentum is conserved across the source-drain interface, a larger range of k_y subtended by the drain EEC translates to a greater number of propagating states which can transmit electrons over a wider range of incidence angle. The transmission peaks occur near $\phi_{M2} = 0, \pi$, which correspond to the two magnetization angles where the drain EECs cover the largest k_y range. In the large M_2 regime shown in Fig. 5(c), the energy gap induced by the in-plane magnetization eliminates the presence of propagating states at $\phi_{M2} = \pm n\pi/6$, $n = (1, 3, 5)$, and reduces the k_y range covered by the drain EECs at other magnetization angles. The absence of propagating states for certain range of ϕ_{M2} leads to a sharp modulation of the transmission about the critical angles of $\phi_{M2} = \pm n\pi/6$, $n = (1, 3, 5)$, a feature which would be conducive for applications to sense the orientation of $\vec{M}_2$, such as memory read-out. The displacement of the drain EECs from the k-space origin also leads to some portions of the drain EECs lying outside the source EEC. This leads to the generally lower transmission seen in Fig. 5 for large values of M_2.

The effects of varying the potential in the drain segment for a fixed magnitude of magnetization provides an alternative perspective. Fig. 6 shows the transmission plotted against the drain magnetization direction and drain potential. The trends observed can also be explained by examining the EEC profiles in the drain region, shown

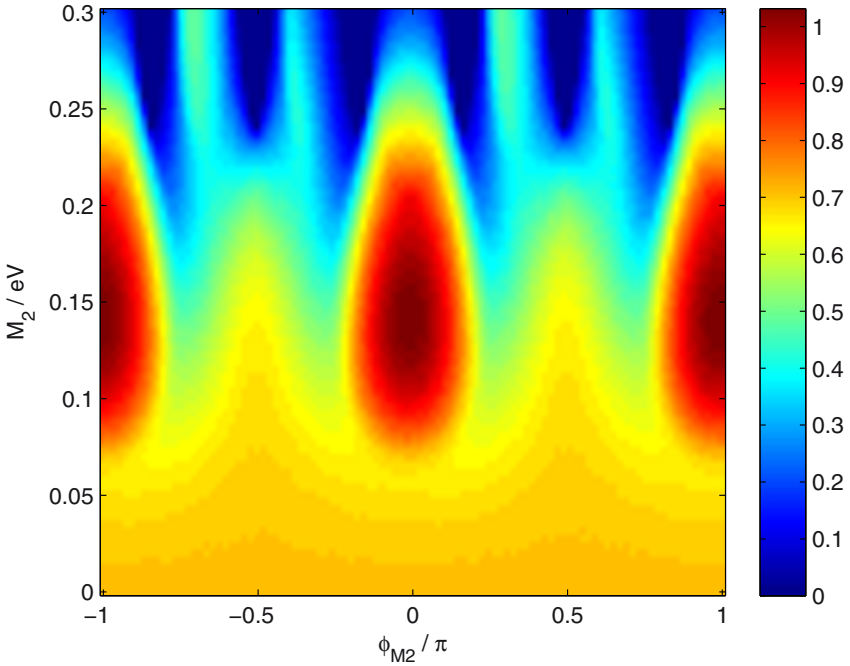

Figure 4 | The transmission plotted against the drain magnetization direction ϕ_{M2} and magnetization magnitude for $E = 0.3$ eV and $E_2 = E - U_2 = 0.1$ eV.

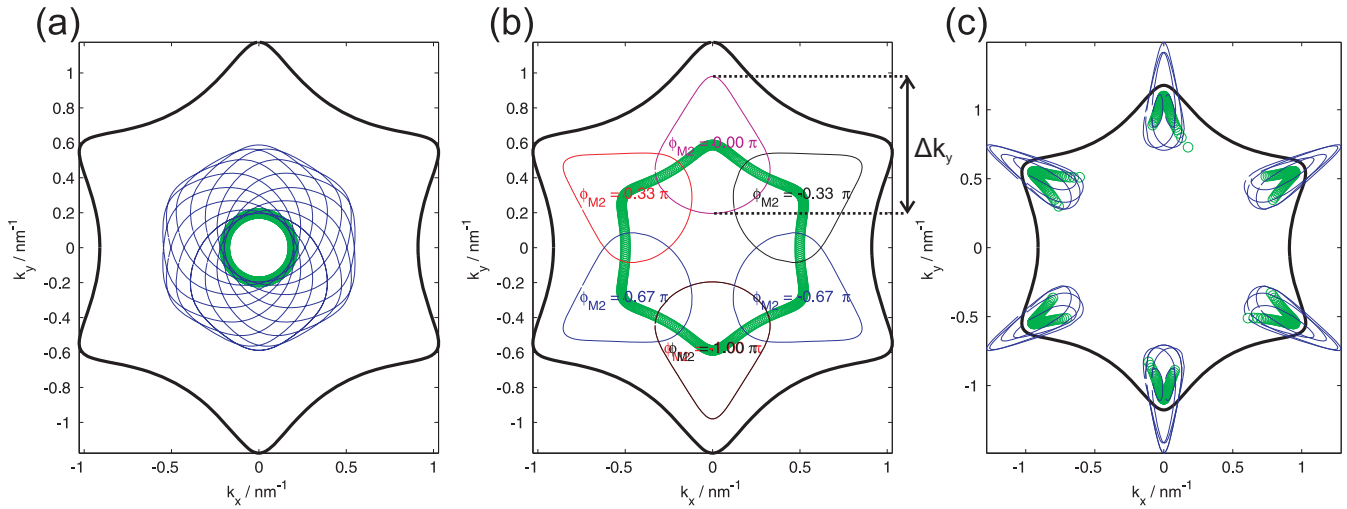

Figure 5 | The EECs in the source region (thick black hexagon) at $E = 0.3$ eV, the trajectories of the Dirac points traced out by ϕ_{M2} by the variation of ϕ_{M2} (thick green lines) and the EECs in the drain region (thin blue lines) for $E_2 = 0.1$ eV and M_2=(a)0.05 eV, (b) 0.15 eV and (c) 0.28 eV. The positions of the Dirac points and the corresponding values of ϕ_{M2} for each of the drain EECs are marked out in (b) in the same color. The k_y range spanned by the $\phi_{M2} = 0$ drain EEC is indicated in panel (b).

for three representative values of E_2 in Fig. 7. The low transmission centered around $\phi_{M2} = n\pi/6$, $n = 1, 3, 5$ at low values of E_2 corresponds to the absence of propagating states due to the large band gaps induced at these values of ϕ_M (Fig. 7(a)). The transmission peaks at $\phi_M = 0, \pi$ at intermediate values of E_2, where the drain EECs still lie largely within the k_y region spanned by the source EEC, correspond to the largest range of k_y spanned by the drain EECs as ϕ_{M2} is varied (Fig. 7(b)). As E_2 is increased further, an increasing proportion of the k-space area spanned by the EECs starts to fall outside the k_y region spanned by the source EEC. This leads to the transmission peaks occurring close to $\phi_M = \pm\pi/2$ where the overlap in the k_y region spanned by both the source and drain EECs is the greatest (Fig. 7(c)).

We have thus far concentrated on the k_y overlap between the source and drain EECs as the primary explanation of the observed transmission profile. However, the k_x and spin mismatch in the source and drain regions does affect the transmission as well. In order to investigate the effects of these two factors, we now let the range of E_2 in Fig. 6 extend to negative values as shown in Fig. 8. Negative values of E_2 correspond to transmission from source particle states to drain hole states, which have the opposite spin configuration.

The general features of the transmission profile for particle-to-particle transmission (positive E_2) are largely similar, but not identical, to those for particle-to-hole transmission. The reason for this lies in the fact that for a given magnetization $\vec{M}$ and $|E|$ the EECs for the particle and hole states with energy $\pm|E|$ have identical shapes. The *right propagating* states for positive and negative values of E, however, lie in different segments of the EECs as shown in panel (b) of Fig. 8. The k_y range spanned by the right propagating states for negative and positive values of E are roughly the same. This accounts

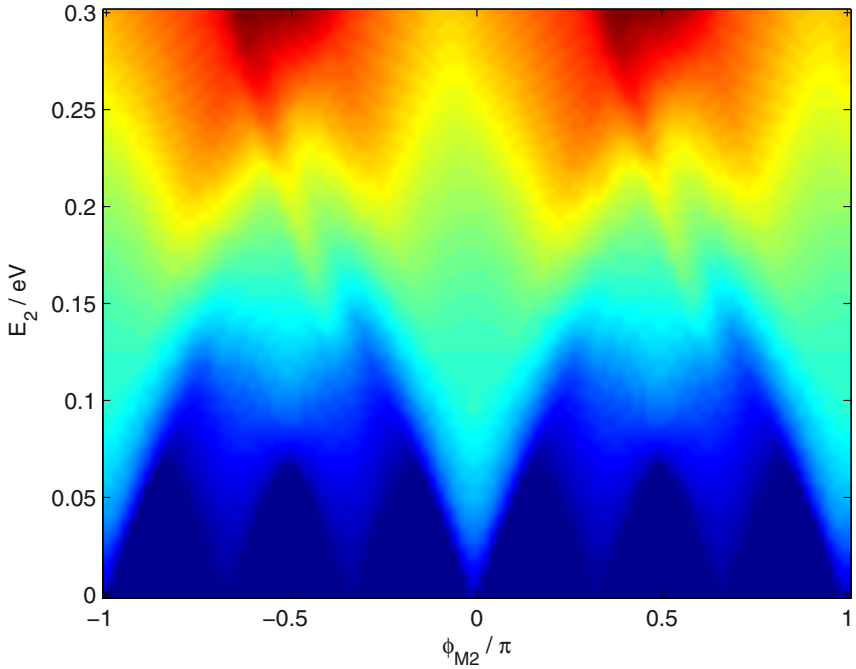

Figure 6 | The transmission plotted against the drain magnetization direction direction ϕ_{M2} and drain energy E_2 for $E = 0.3$ eV and $M_2 = 0.2$ eV.

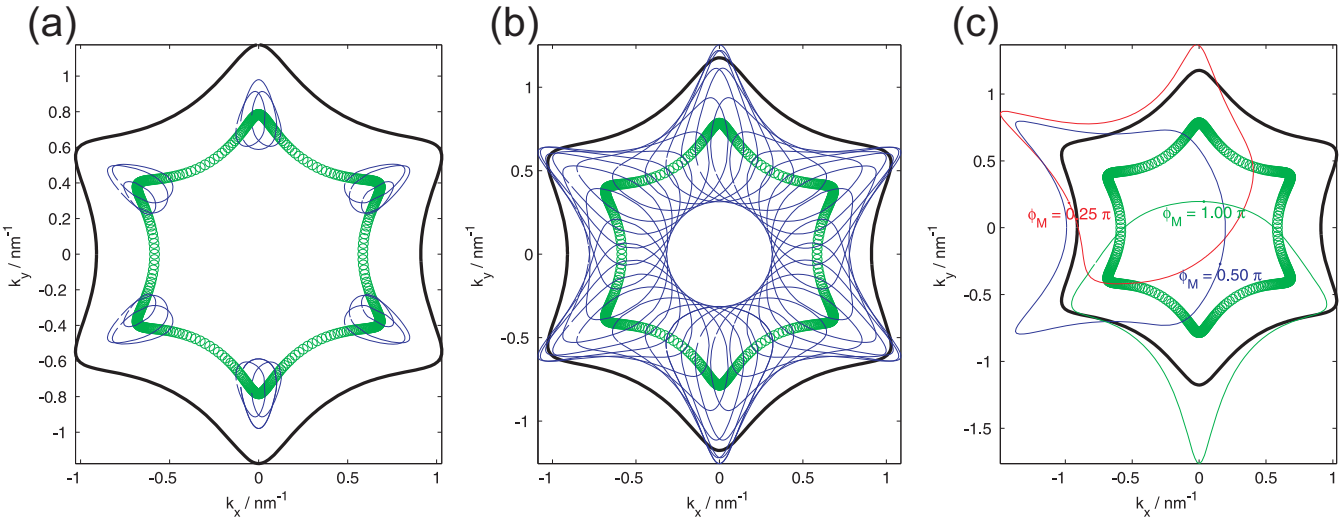

Figure 7 | The EECs in the source region (thick black hexagon) at $E = 0.3$ eV, the trajectories of the Dirac points traced out by the Dirac points (thick green lines) by the variation of ϕ_{M2} (green dots) and the EECs (thin blue lines) in the drain region for $M_2 = 0.1$ eV, and E_2=(a)0.05 eV, (b) 0.12 eV and (c) 0.25 eV.

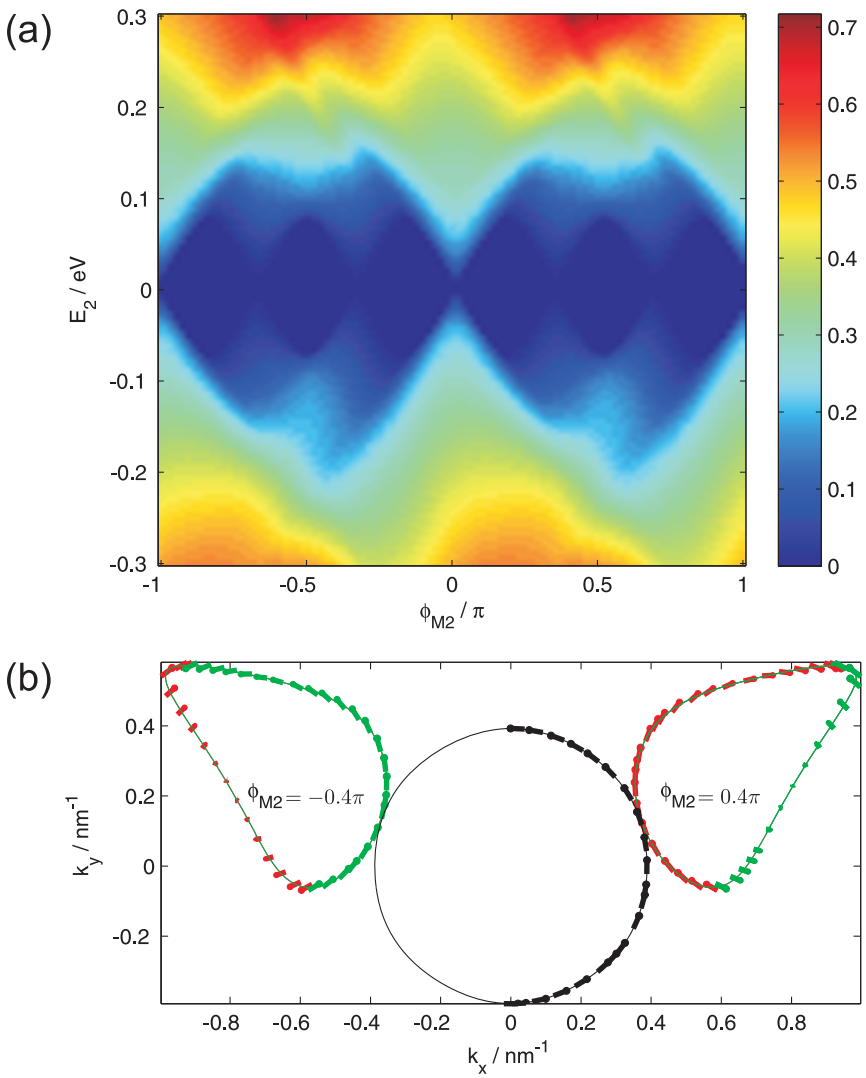

Figure 8 | (a) The transmission profile for the same set of parameters as in Fig. 6 with the exception that E_2 now extends to negative values. (b) The EECs for an unmagnetized segment at $E = 0.1$ and no magnetization (black), and $M_2 = 0.2$ eV, $\phi_{M2} = 0.4\pi$ and $\phi_{M2} = -0.4\pi$ respectively as labeled. The arrows indicate the directions of the in-plane spin polarization on the EECs of the right propagating hole (green) and particle (red) states in the drain segment. The lengths of the arrowheads are indicative of the magnitude of the in-plane spin polarization.

for the similarities in the particle-to-particle and particle-to-hole transmission profiles in terms of the rough positions of the transmission peaks and troughs. However, the difference in the k_x values and spin orientations of the right propagating states of electrons and holes leads to the asymmetry in the particle-to-particle and particle-to-hole transmission profiles. This asymmetry is accentuated by the distortion of the constant energy surfaces from the circular shape by the hexagonal warping term. In addition, there is also an asymmetry in the transmission profile about the $\phi_{M2} = 0$ axis. This may be explained by considering the EECs for $\pm\phi_M$, for some given ϕ_M. As shown in Fig. 8(b), the EECs for $\pm\phi_M$ are reflections of each other about the $k_x = 0$ axis. However, the portions of the EECs which correspond to the right propagating states lie on different regions of the corresponding EECs for $\pm\phi_M$. This leads to, for instance, the right propagating states at a given value of k_y having different spin polarizations for opposite signs of ϕ_M, and hence an asymmetrical transmission profile about $\phi_{M2} = 0$. Thus, in summary, two factors play a role in determining the dependence of the transport on the magnetization direction and magnitude – the extent of the overlap across k_y of the the source and drain EECs, and the degree of mismatch between the spin configurations of the propagating states in the two electrodes.

We note in passing that proposals for the formation of the Majorana fermion state in TI systems involve junctions between ferromagnetic insulators and superconductors deposited on top of TIs. The anisotropy in the shape of the EECs induced by the in-plane magnetization and asymmetry between the particle and hole states just discussed may lead to the presence of Majorana fermion states in Bi_2Te_3 with unusual properties compared to Majorana states resulting from TIs with the more commonly studied circular EECs. The anisotropy may also be indicative of anomalous effects which emerge as the dimensions of the TI segments are shrunk from being semi-infinite (in the x and z directions) to finite ones[18]. A detailed discussion of these issues are, however, beyond the scope of this paper.

Conclusion

In this work we showed the appearance of a band gap, and the accompanying distortion and displacement of the constant energy curves in k space in Bi_2Te_3 with the application of an in-plane magnetic field. We then studied the transmission to a drain Bi_2Te_3 segment with an external magnetization and potential applied from a source Bi_2Te_3 segment without the magnetization and potential. The band gap, and distortion and displacement of the constant energy curves by the in-plane magnetization affects the overlap of the transverse momentum k_y range spanned by the EECs in the source and drain regions. The sharp modulation of the transmission with the magnetization orientation for the high M_2 regime and low E_2 regime, as depicted in Figs. 4 and 6, respectively, suggests a possible application of Bi_2Te_3 in the read-out of magnetic memory. The two states of a memory bit can be represented by the magnetization direction of an adjoining ferromagnetic layer (which is coupled to the topological surface states of Bi_2Te_3) being in the $\phi_M = 0$ and $\phi_M = \pi/2$ directions. In the former state there is no band gap and the transmission is finite while in the latter the transmission is 0 due to the large band gap. A gate voltage can be applied on the drain segment to tune the value of E_2 so as to achieve an optimum balance between the differences in transmission between the two memory states, and the robustness of the system to deviation of the magnetization from the reference $\phi_M = 0$ and $\phi_M = \pi/2$ directions.

1. Hasan, M. Z. & Kane, C. L. Colloqium: Topological insulators. *Rev. Mod. Phys* **82**, 3045 (2010).
2. Fu, L. & Kane, C. L. Superconducting proximity effect and majorana fermions at the surface of a topological insulator. *Phys. Rev. Lett* **100**, 096407 (2008).
3. Yokoyama, T., Tanaka, Y. & Nagaosa, N. Manipulation of the Majorana fermion, Andreev reflection, and Josephson current on topological insulators. *Phys. Rev. Lett* **103**, 107002 (2009).
4. Linder, J., Yukio, T., Yokoyama, T., Sudbø. & Nagaosa, N. Unconventional superconductivity on a topological insulator. *Phys. Rev. Lett* **104**, 067001 (2010).
5. Yokoyama, T., Zang, J. & Nagaosa, N. Theoretical study of the dynamics of magnetization on the topological surface. *Phys. Rev. B* **81**, 241410(R) (2010).
6. Burkov, A. A. & Hawthorn, D. G. Spin and charge transport on the surface of a topological insulator. *Phys. Rev. Lett* **105**, 066802 (2010).
7. Taguchi, K., Yokoyama, T. & Tanka, Y. Giant magnetoresistance in the junction of two ferromagnets on the surface of diffusive topological insulators. *Phys. Rev. B* **89**, 085407 (2014).
8. Yokoyama, T., Tanaka, Y. & Nagaosa, N. Anomalous magnetoresistance of a two-dimensional ferromagnet/ferromagnet junction on the surface of a topological insulator. *Phys. Rev. B* **81**, 121401(R) (2010).
9. Hsieh, D. *et al.* A tunable topological insulator in the spin helical Dirac transport regime. *Nature* **460**, 1101–1105 (2009).
10. Chen, Y. L. *et al.* Experimental Realization of a Three-Dimensional Topological Insulator, Bi_2Te_3. *Science* **325**, 178–181 (2009).
11. Fu, L. Hexagonal Warping Effects in the Surface States of the Topological Insulator Bi_2Te_3. *Phy. Rev. Lett.* **103**, 266801 (2009).
12. Hassler, F., Akhmerov, A. R. & Beenakker, C. W. J. Flat-lens focusing of electrons on the surface of a topological insulator. *Phys. Rev. B* **82**, 125423 (2010).
13. Henk, J. *et al.* Topological Character and Magnetism of the Dirac State in Mn-Doped Bi_2Te_3. *Phys. Rev. Lett.* **109**, 076801 (2012).
14. Wang, J. *et al.* Power-law decay of standing waves on the surface of topological insulators. *Phys. Rev. B* **84**, 235447 (2011).
15. An, J. & Ting, C. S. Surface states scattering from a step defect in the topological insulator Bi_2Te_3. *Phys. Rev. B* **86**, 165313 (2012).
16. Zhang, D. & Ting, C. S. Impact of step defects on surface states of topological insulators. *Phys. Rev. B* **85**, 115434 (2012).
17. Rakyta, P., Pályi, A. & Cserti J. Electronic standing waves on the surface of the topological insulator Bi_2Te_3. *Phys. Rev. B* **86**, 085456 (2012).
18. Linder, J., Yokoyama, T. & Sudbø, A. Anomalous finite size effects on surface states in the topological insulator Bi_2Se_3. *Phys. Rev. B* **80**, 205401 (2009).

Acknowledgments

We thank the National Research Foundation of Singapore under the Competitive Research Program "Non-Volatile Magnetic Logic And Memory Integrated Circuit Devices" NRF-CRP9-2011-01 for financial support.

Author contributions

Z.B.S. performed the calculations and wrote the main manuscript text, and M.B.J. and S.G.T. verified the theoretical derivations and contributed to the discussion section. All authors reviewed the manuscript.

Additional information

Competing financial interests: The authors declare no competing financial interests.

How to cite this article: Siu, Z.B., Jalil, M.B.A. & Tan, S.G. Topological state transport in topological insulators under the influence of hexagonal warping and exchange coupling to in-plane magnetizations. *Sci. Rep.* **4**, 5062; DOI:10.1038/srep05062 (2014).